scientific reports

Check for updates

OPEN

The effect of non-stoichiometry in Sb_2Se_3 films on their phonon and electronic properties in the infrared range

Bohdan Andriyevsky[1]✉, Leszek Bychto[1], Aleksy Patryn[1], Takhir Razykov[2], Bobur Ergashev[2], Kudratulia Kouchkarov[2], Ramozan Khurramov[2], Diyorbek Isakov[2], Mukhammad Pirimmatov[2], Ulrich Schade[3], Florian Ruske[4], Alexander Steigert[4], Rene Schwiddessen[4], Ljiljana Puskar[3], Alexander Veber[3,5], Andrii I. Kashuba[6] & Michał Piasecki[7]✉

Due to the noticeable part of Sb_2Se_3 films in solar cell technology, the deposition of Sb_2Se_3 films with the desirable content and improved crystalline perfection is of crucial importance. Therefore, extensive experimental and theoretical studies of the electronic and phonon properties of these materials are of interest. In this work, the stoichiometry and morphology of antimony selenide films are correlated to their optical properties in the far-infrared regime and compared to theoretically calculated properties for an ideal crystal. For this study, the reflectance of a series of 1.4–1.7 µm thick Sb_xSe_y layers, produced on soda-lime glass substrates by molecular beam chemical deposition, was measured in the spectral range of 25–5000 cm^{-1} using an FT-IR spectrometer and synchrotron radiation. The near-surface and bulk crystallographic structure and phase composition were previously determined using grazing incidence X-ray diffraction (GIXRD) under varying incident angles. The chemical composition and morphology were investigated using scanning electron microscopy (SEM) and energy-dispersive X-ray spectroscopy (EDX). It was shown that the spectral positions of numerous maxima of the reflectance of Sb_xSe_y layers for various x/y indices in the phonon excitation range of 25–230 cm^{-1} are consistent with the positions of the maxima of the imaginary part of the dielectric function of Sb_2Se_3 crystals, calculated within the framework of density functional theory. A significant increase in the reflectance values was observed for Sb_xSe_y layers containing the largest relative amount of antimony *x/y*, which may be due to the increased content of the metallic form of antimony compared to the amount of the pure Sb_2Se_3 semiconducting phase. A correlation was found between the technological parameters of production (temperature) and the final chemical composition and morphology of the Sb_xSe_y layers. To explain the observed relationships, calculations of the cohesive energy of Sb_2Se_3 and Sb crystals and the binding energy of the residual antimony atom inside and on the surface of the antimony selenide supercell were performed. The main conclusions of the theoretical calculations are consistent with the results of EDX and XRD measurements of the Sb_xSe_y layers.

Keywords Sb_xSe_y films, Sb_2Se_3 crystal, Phonon spectra, Electron properties

Antimony selenide (Sb_2Se_3) is a compound semiconductor that has been proposed as an absorber for thin film solar cells since it possesses a number of useful properties for photovoltaic application, such as a simple chemical

[1]Faculty of Electronics and Computer Sciences, Koszalin University of Technology, Śniadeckich str. 2, 75-453 Koszalin, Poland. [2]Physical-Technical Institute of Uzbekistan Academy of Sciences, Chingiz Aytmatov 2B, 100084 Tashkent, Uzbekistan. [3]Institute for Electronic Structure Dynamics, Helmholtz-Zentrum Berlin für Materialien und Energie GmbH, Albert-Einstein-Strasse 15, 12489 Berlin, Germany. [4]Solar Energy Division, Helmholtz-Zentrum Berlin für Materialien und Energie GmbH, Kekuléstraße 5, 12489 Berlin, Germany. [5]Department of Chemistry, Humboldt Universität zu Berlin, Brook-Taylor-Straße 2, 12489 Berlin, Germany. [6]Department of General Physics, Lviv Polytechnic National University, Bandera str. 12, Lviv 79013, Ukraine. [7]J. Dlugosz University Częstochowa, Armii Krajowej 13/15, 42200 Częstochowa, Poland. ✉email: bohdan.andriyevskyy@tu.koszalin.pl; m.piasecki@ujd.edu.pl

composition, an optimal band gap (1.2 – 1.3 eV), a large absorption coefficient, and a quasi-one-dimensional crystal structure[1,2]. Despite silicon being the dominant absorber material in photovoltaics, chalcogenides like CdTe and Cu(In, Ga)Se_2 or metal-halide Perovskites have been extensively studied as absorber materials and led to solar cell efficiencies exceeding 20%[3–5]. However, the instability of halide perovskites, high toxicity of Pb and Cd, high cost and low abundance of Ga and In, and the high consumption of materials and energy in the production process of crystalline silicon stimulate research aimed at finding alternative, easy-to-synthesize, inexpensive, and environmentally friendly photovoltaic materials[6–9]. Antimony selenide, Sb_2Se_3, could be an alternative to the established chalcogenides due to many advantages, including low toxicity, earth abundance, phase stability, and simple binary structure[6,10,11]. Just recently, the 4-terminal tandem solar system with a Sb_2Se_3 bottom cell and a Perovskite top cell has been demonstrated, exhibiting total efficiency also exceeding 20%[12].

The band gap E_g = 1.01–1.2 eV, high absorption coefficient $\alpha > 10^5$ cm^{-1}, low melting point, and high partial pressure make it possible to grow high-quality Sb_xSe_y films at relatively low temperatures[13]. The quasi-one-dimensional structure of Sb_2Se_3 consists of covalently bonded $(Sb_4Se_6)_n$ elements along one crystallographic direction. In two other orthogonal directions, these elements are stacked by weak van der Waals forces[14]. As a result, strong anisotropic optoelectronic properties, such as preferential carrier transport in the direction along the covalently bonded ribbons, take place. Thus, by changing the crystalline orientation of the Sb_2Se_3 films, it is possible to change the carrier mobility, which can potentially improve photovoltaic performance[15].

It has recently been shown[1] that Sb_xSe_y does not allow for obtaining a spatially homogeneous crystal with a composition showing a large deviation from stoichiometry, but rather prefers a decomposition into the Sb_2Se_3 phase and the secondary Sb or Se phases[1].

According to the results of Ref.[16], the electrical conductivity of non-stoichiometric Sb_xSe_y films increases drastically as a function of *x*/*y* ratio in the range of 0.7 - 0.9, and, at the same time, the *p*-type of conductivity changes to the *n*-type. The formation and nature of defects such as (V_{Sb1}, V_{Sb2}, Se_{Sb1}, Se_{Sb2}, $2Se_{Sb1}$, $2Se_{Sb2}$) in Se-rich films, and (V_{Se1}, V_{Se2}, V_{Se3}, Sb_{Se1}, Sb_{Se2}, Sb_{Se3}) in Sb-rich films have been investigated[17,18]. These studies revealed that V_{Sb1} and V_{Sb2} defects in Se-rich films, as well as V_{Se2} and V_{Se3} defects in Sb-rich films, result in the appearance of deep levels inside the band gap of thin films, acting as recombination centers. Additionally, Se_{Sb1}, Se_{Sb2}, $2Se_{Sb1}$, and $2Se_{Sb2}$ form acceptor traps in Se-rich films, while Sb_{Se1} and V_{Se1} defects result in shallow donor levels in Sb-rich films. According to recent results[19], the loss of selenium atoms in deposited Sb_2Se_3 thin films has been detected, which causes V_{Se} defects and has important implications for the device performance, especially in terms of charge recombination and optical spectral response. From the analysis of reference data, it is clear that despite relatively small changes in the band gap of Sb_2Se_3-based compounds, stoichiometric deviations have a significant impact on the electronic properties of Sb_xSe_y films[19].

Optical properties of the antimony selenide films are crucial for the construction of the corresponding solar cells. In Ref[20]., the measured bandgap of the film was found to be $E_{g,\,i}$ = 1.16 eV, formed by the indirect optical transitions. The complex dielectric function $\varepsilon(\nu) = \varepsilon_1(\nu) + i\varepsilon_2(\nu)$ of Sb_2Se_3 crystal calculated from first principles (using Wien 2k code) in the range of electron excitations 0–25 eV reveals clear optical anisotropy, resulting from the anisotropy of chemical bonding in the crystal. The dielectric permittivities $\varepsilon_1(\nu=0)$ were obtained to be $\varepsilon_1^{(x)} = 15.18$, $\varepsilon_1^{(y)} = 21.72$, $\varepsilon_1^{(z)} = 22.31$.

Authors of Ref[2]. found that polycrystalline c-Sb_2Se_3 is an intrinsically indirect bandgap ($E_{g,\,i}$) material with the lowest $E_{g,\,i}$ of 1.03 ± 0.01 eV and the lowest direct bandgap ($E_{g,\,d}$) of 1.17 ± 0.02 eV at 300 K. The relative dielectric permittivity at infinite frequency ε_∞ of the c-Sb_2Se_3, 13.7–26 and 80–133 at zero frequency (ε_0), has been reported by different authors[21–24]. The optical edge of the amorphous antimony selenide, a-Sb_2Se_3, was measured as 1.39 ± 0.02 eV by ellipsometry (the optical edge for amorphous materials is analogous to the bandgap for crystals)[2].

In the paper[12], the antimony selenide films deposited on Si/SiO_2 (100) substrates using molecular beam evaporation have been investigated. The authors detected the red shift of the band gap E_g with the increase of evaporation temperature, which can be attractive for tuning the photovoltaic characteristics of such films. In that work, the loss of selenium atoms in Sb_2Se_3 was also confirmed through the blue shifts of the Raman peaks.

Given the growing interest in Sb_2Se_3-based films and the expected expansion of their potential photoelectronic applications, in-depth theoretical and experimental studies linking their properties to stoichiometry, crystal structure, and morphology remain important. The overall goal of this study is to link the chemical composition to the measured optical properties of Sb_xSe_y thick films in the infrared spectral range as well as to compare the experimental results with theoretical results calculated for an ideal Sb_2Se_3 crystal.

For this purpose we first investigate the influence of deposition conditions in molecular beam chemical deposition of Sb_xSe_y onto soda-lime glass using separate sources for Sb and Se, respectively, onto the chemical, morphological and phase composition of the resulting films. Using reflectance measurements we investigate the phonon and electronic structure of the synthesized materials using synchrotron radiation. Results of the series of synthesized Sb_xSe_y thick films of varying stoichiometry are compared to a reference Sb_2Se_3 crystal. To clarify the observed relationships, we will compare the experimental data obtained for the Sb_xSe_y thick films with the theoretically calculated properties. The experimental far-infrared reflection spectra of the films can be compared relatively easily with the theoretical dielectric function calculated by first-principle density functional theory (DFT) methods. Besides, the far-infrared reflection and/or absorption method, when applied to Sb_2Se_3 films, can deliver information on the free electron/hole carriers in the films.

Deposition, microstructure and chemical composition of Sb_xSe_y films

The initial masses/weights of Sb and Se and the corresponding atomic contents used for Sb_xSe_y film deposition (Fig. SD-1 of Supplementary designation) are presented in Table 1. As it is known that selenium atoms can easily escape from the growing film, the growth conditions were varied with increasing Se rate to find optimum conditions for stoichiometric films. Thus, the indices *x*/*y*, corresponding to the relative atomic contents of

Deposition characteristics						Initial masses		Masses and atomic number relations	
1	2	3	4	5	6	7	8	9	10
Sample No.	T_{SLG} /°C	T_{Sb} /°C	T_{Se} /°C	Evaporation time /min	Thickness /µm	m_{Sb} /mg	m_{Se} /mg	m_{Sb}/m_{Se}	N_{Sb}/N_{Se} (x/y)
1	450	950	430	30	1.5	48	79	0.61	0.375
2	450	950	435	30	1.7	49	118	0.41	0.257
3	450	940	440	30	1.7	14	150	0.093	0.0577
4	450	952	434	30	1.5	56	107	0.52	0.323
5	450	960	410	30	1.4	73	60	1.22	0.752
6	450	960	420	30	1.6	70	68	1.03	0.636
7	450	955	430	30	1.7	61	78	0.78	0.483
8	450	950	420	30	1.6	47	68	0.69	0.427

Table 1. Deposition characteristics, initial masses, and masses and atomic number relations of Sb_xSe_y films deposited on the soda-lime glass substrates. The indices x and y are obtained by dividing the masses of Sb and se components m_{Sb} and m_{Se} (columns 7 and 8) by the corresponding atomic masses $\mu_{Sb} = 127.76$) and $\mu_{Se} = 78.971$.

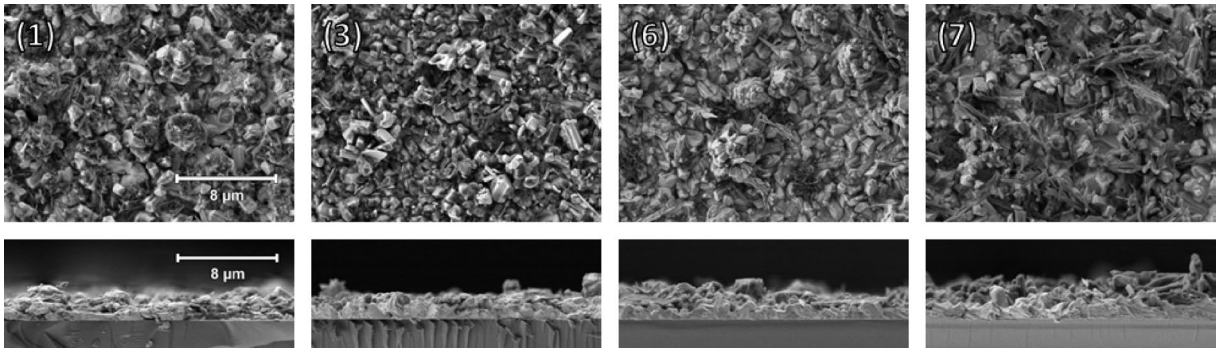

Fig. 1. Microstructures of Sb_xSe_y films deposited on soda-lime glass substrates in top view and cross-sectional view. The numbers correspond to the nominations in Table 1.

antimony and selenium initial components, were chosen to be much smaller than the theoretical value 0.67 (see last column of Table 1). Our goal was to obtain Sb_2Se_3 thick films with stoichiometric composition at high substrate temperatures by controlling the temperature of individual sources. The substrate temperature used was kept at T_{SLG} = 450 °C, which is a bit higher than the critical temperature T = 423 °C, at which the evaporation of the deposited Sb_2Se_3 films was detected in vacuum ($P = 5 \times 10^{-4}$ Pa)[25]. Thus, a more intense loss of selenium atoms was probable compared to the loss of antimony ones during the deposition of Sb_xSe_y films on SLG substrates.

The morphological and structural properties of the films were studied by scanning electron microscopy (SEM) and X-ray diffraction (XRD), while the atomic content of the deposited Sb_xSe_y films was studied by using Energy Dispersive *X*-ray Spectroscopy (EDX). For SEM and EDX, a Zeiss MERLIN field emission SEM with an Oxford Instruments Ultim Extreme detector was used. Imaging was performed at an acceleration voltage of 3 kV and using an Everhart-Thornley detector to highlight the morphology of the samples. For EDX measurements, an acceleration voltage of 10 kV was used in order to sufficiently excite L-line X-ray emission from Sb atoms. XRD measurements were performed on a Bruker D8 Advance in grazing incidence at incident angles of 1°, 5°, and 10°.

Top view and cross-sectional SEM images of selected Sb_xSe_y films are presented in Fig. 1 (top view of all samples in higher magnification is shown in Fig. SD-2 of Supplementary designation). The films show quite significant variation in surface topography. Depending on the sample, we can observe elongated needle-like structures, presumably crystalline, large, presumably crystalline, grains with diameters in the µm-range and additional phases in between and on top of said grains with unclear morphology and possibly amorphous nature. From investigations on different locations on the samples, it seems the topography is similar on different locations. Cross-sectional views confirm the high roughness of the films and show that some features of the films pile up to a thickness above 3 µm, while the thickness values given in Table 1 are reasonable average values.

EDX analysis confirms the presence of Se, Sb, Na, O, and C (see Figs. SD-3 and SD-4 of Supplementary designation). While carbon is commonly observed on many samples as a surface contaminant, it is unclear whether oxygen originates from oxide phases or contamination as well. We can rule out the glass substrate as an oxygen source in most cases, as the Si line is only observed on very few spectra, most likely due to pinholes

or very thin film areas, while in general, the films were thick enough to prevent excitation of the glass substrate. Additionally, S and Cl can be seen in small quantities for a few spots, again, most likely not as film constituents but contamination.

All films, however, show a rather clear sodium signal. It is well known, for instance from preparation of CIGS (Cu(In, Ga)Se_2) thin film solar cells, that Na shows substantial diffusion from the glass substrate into the growing film[26,27]. While the substrate temperatures in CIGS growth are slightly above the temperatures used in our study, we grew the investigated films directly on the glass substrate, and soda-lime glass contains enough Na to explain the measured quantities. Thus, out-diffusion from the glass is a possible origin for the high Na content inside the films.

As the films do not meet the requirements for a reliable quantification, namely a flat surface and a homogeneous distribution of elements, we merely use the quantification results to compare the ratio of Sb to Se for different films. Absolute values must be regarded as a rough estimate, but can be used to compare samples relative to each other. In order to minimize the effects of potential lateral inhomogeneity, the EDX spectra were collected at a rather low magnification on an area of approximately 85 by 115 µm. This was repeated at 3 locations on the samples in order to check the reproducibility of the measurement.

We observe mediocre reproducibility despite identical measurement conditions on different locations at the substrate. The differences observed for measurements on different locations of the same film is however smaller than the differences between some of the samples (Fig. 2a). The accuracy of the quantification does not suffice to lead to exact numbers, but we can identify samples with more metallic characteristics than others (Fig. 2b). Sample 1 is most metallic, samples 2, 5 and 6 also seem to contain excess antimony. All other films seem to be close to stoichiometry.

We have used the determined relative concentrations c(Sb)/c(Se) (Fig. 2b) for the study of the correlation of this value with the source temperatures T_{Sb} and T_{Se} during the film deposition. As a result, weak but clear correlations of the value c(Sb)/c(Se) with the source temperatures T_{Sb} and T_{Se} are found (Fig. 3). These correlations permit us to estimate the necessary source temperatures T_{Sb} and T_{Se} to obtain the deposited layer of the desired concentration c(Sb)/c(Se). According to the linear approximations of the dependences in Fig. 3, the source temperatures corresponding to the stoichiometric content of Sb_xSe_y films (Sb_2Se_3) are T_{Sb} = 952 °C and T_{Se} = 426 °C.

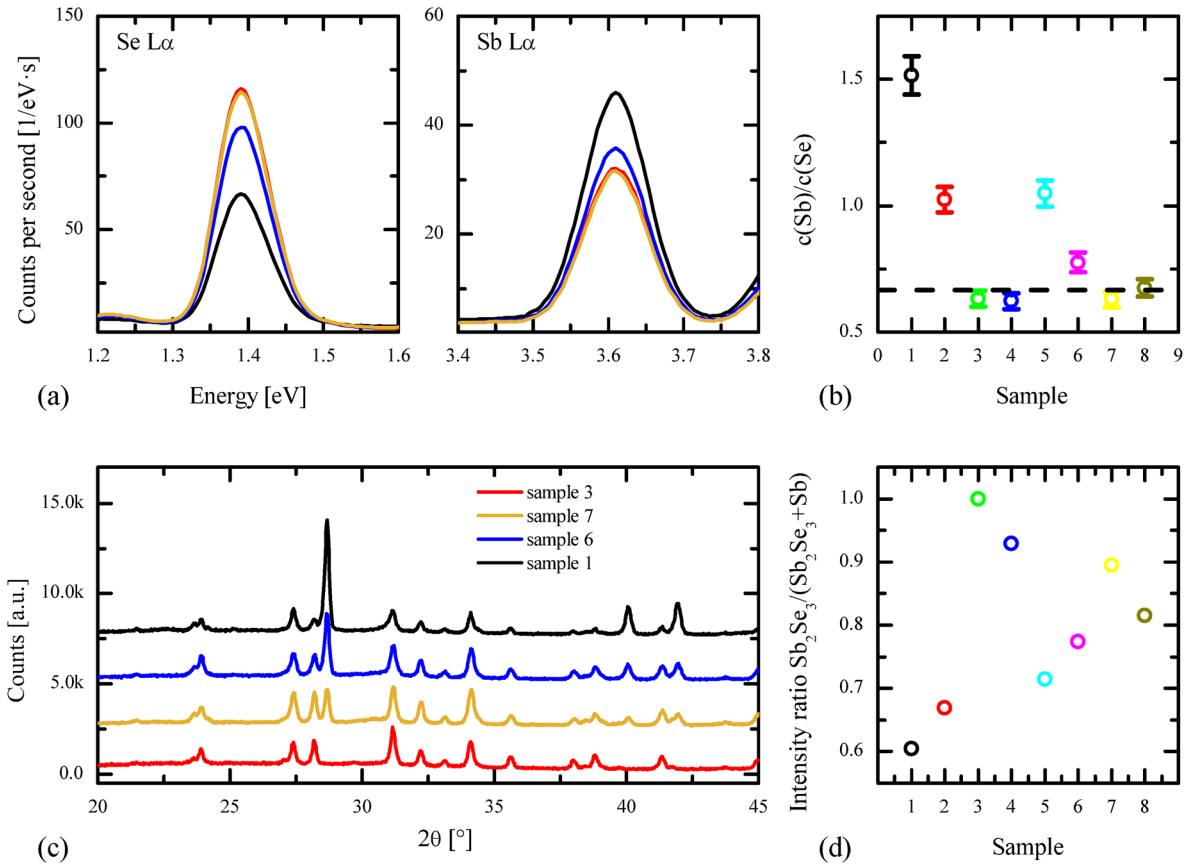

Fig. 2. (a) Zoom into the EDX spectra on the main Se and Sb emission lines for a subset of samples with different stoichiometry, (b) ratio of atomic concentrations c(Se)/c(Sb) as determined by standardless quantification of measured EDX spectra, (c) X-ray diffraction patterns obtained in grazing incidence mode with an incident angle of 5° for the same set of samples as in panel (a), and (d) relative contribution of the stoichiometric Sb_2Se_3 phase to all observed phases obtained by refinement of GIXRD patterns (see main text).

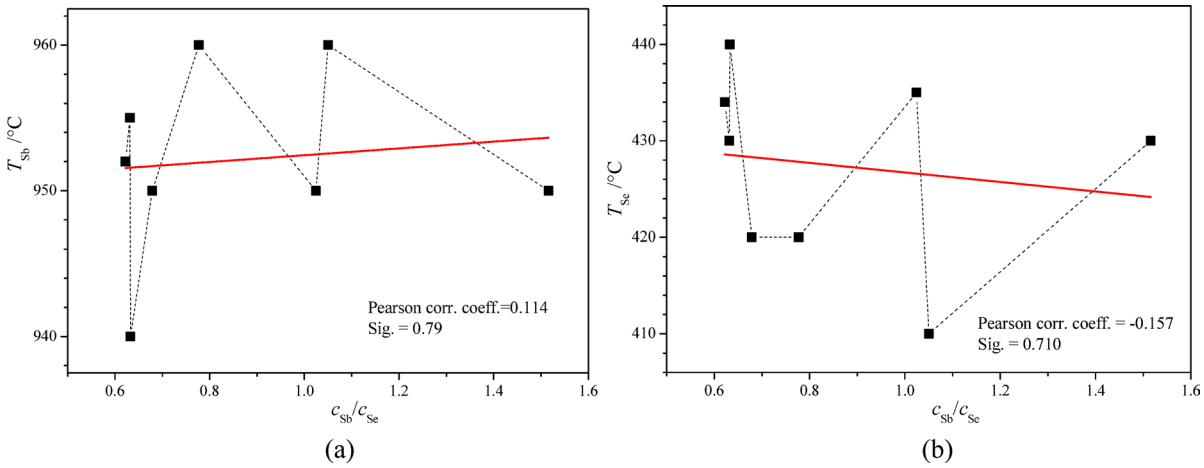

Fig. 3. Relations between antimony (a) and selenium (b) source temperatures T_{Sb} and T_{Se} during Sb_xSe_y film deposition and their relative concentration c_{Sb}/c_{Se} determined from SEM measurements. Direct lines are the linear approximations of the corresponding dependences.

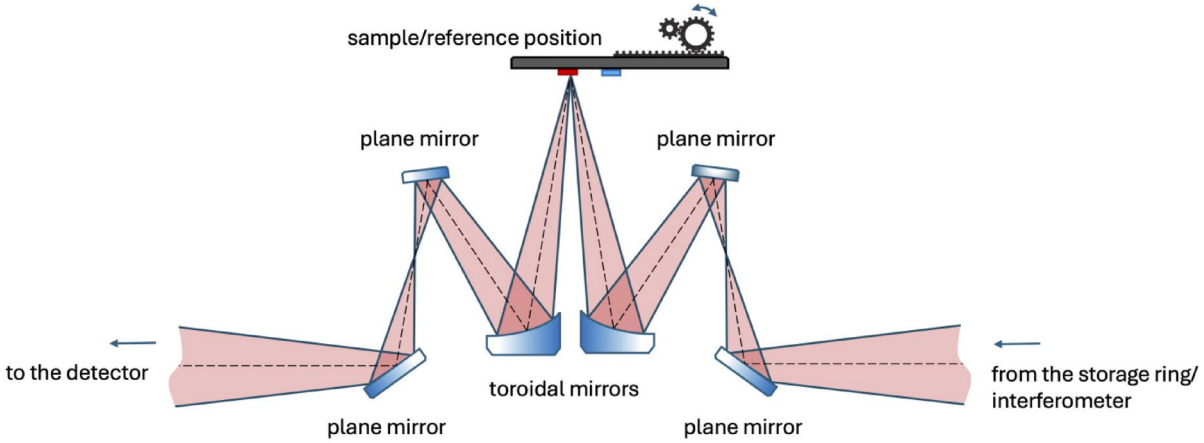

Fig. 4. Optical scheme for the reflection spectra measurement of Sb_xSe_y films using FT-IR spectrometer at IRIS beamline of BESSY II storage ring.

In order to further check the results from EDX measurements, we complemented the analysis with XRD measurements (Fig. SD-5 of Supplementary designation). Examples of diffraction patterns collected in grazing incidence (GI) at an incident angle of 5° are shown in Fig. 2c, along with the position of diffraction peaks of metallic antimony taken from the literature. Le Bail refinements on all GI diffraction patterns (Figs. SD-6, SD-7 and SD-8 of Supplementary designation), under all three different angles used, prove that all peaks can be either attributed to the metallic Sb phase or the compound phase Sb_2Se_3.

All samples consist of both the Sb_2Se_3 and the metal phase, except for sample 3, which seems to be pure Sb_2Se_3. In Fig. 2(d), we plot the ratio of the Sb_2Se_3 contribution to the diffraction pattern to the overall crystalline contributions found. The value should not be understood as a volumetric or weight contribution of both phases, but rather as a means to compare samples to each other. We find this intensity ratio to nicely correspond to the EDX results; however, we find XRD to be more sensitive to finding residual pure metal for samples close to ideal stoichiometry.

Methods of reflection spectra measurements and theoretical calculations

The reflection spectra of Sb_xSe_y films were measured using the optical setup shown in Fig. 4, in the spectral range of 25–5000 cm^{-1}. The high brilliance of the HZB BESSY synchrotron radiation together with a Fourier-transform infrared (FTIR) Bruker Vertex 70/v spectrometer allows for a precise measurement of reflection spectra of the samples by applying a quasi-normal incidence set-up, at the incidence angle of about 8° and with an opening angle of about 50 msr (Fig. 4) as is described in[28] with a gold film as reference. Measurements were performed with undefined polarization of the radiation due to the isotropy of the deposited films. The measurements were done under low-vacuum conditions to avoid the infrared absorption by the residual gases. Spectra were collected using a transition edge superconducting bolometer (QNbTES, QMC, UK) in the spectral range between 20 and

650 cm^{-1} and with the pyroelectric DLaTGS detector in the spectral range between 400 and 5000 cm^{-1}, with a resolution of 4 cm^{-1}.

The reflection spectra of our samples are the result of the reflections from the vacuum-film interface and the reflections from the film-substrate interface. Due to the relatively small Sb_xSe_y film thicknesses ($d \approx 1.5$ µm), the reflection spectra measured may also contain the substrate features. However, in the spectral range 20–300 cm^{-1} of phonon excitations of Sb_xSe_y, no spectral structure of the absorption coefficient of soda-lime glass substrates is observed. According to the reference data on the optical constants n and k of soda-lime glass[29], the absorption coefficient $\alpha = 4\pi k\lambda^{-1}$ (in the present work, the wave number $1/\lambda = \lambda^{-1}$ is denoted by ν) of SLG in the far-infrared range, 30 $cm^{-1} < \nu < 200$ cm^{-1}, increases monotonously with ν. Thus, the features of the optical properties of soda-lime glass substrates in the range of phonon excitations, 20–200 cm^{-1}, are not expected to distort the bulk optical spectra of Sb_xSe_y films. SLG substrates are also transparent in the frequency spectral range of 1200 5000 cm^{-1}[29]. Due to the small thickness of the deposited films, the reflection spectra may not exhibit all expected complex reflection features, as observed in the bulk material, but rather may reveal a combination of the film's and substrate's features.

The DFT calculations of the crystals studied were performed using the VASP code[30–35] with the PAW_PBE pseudopotentials[36]. The exchange-and-correlation functionals PE (PBE) and PS (PBEsol) based on the generalized gradient approximation (GGA)[36] have been used. The dielectric functions in the range of phonon excitations ε(ν) (here ν is a frequency) were calculated within the framework of the density-functional-perturbation theory (DFPT). A cut-off energy for the plane waves of 500 eV, a Methfessel–Paxton smearing of 0.05 eV[37] and 20 irreducible K-points of the K-point spacing 0.2 $Å^{-1}$ were used for the calculations. The relaxations of the electronic and ionic degrees of freedom were performed with the following default VASP stopping criteria: EDIFF = $1 \cdot 10^{-6}$ eV, EDIFFG = $5 \cdot 10^{-3}$ eV. For calculations of the phonon frequencies and dielectric permittivity of the materials studied the stopping criteria were chosen to be two orders of magnitude smaller: EDIFF = $1 \cdot 10^{-8}$ eV, EDIFFG = $5 \cdot 10^{-5}$ eV.

The crystal structure of Sb_2Se_3 belongs to the orthorhombic space group of symmetry *Pnma* (no. 62). The elementary unit cell of Sb_2Se_3 of the dimensions $a = 1.18$ nm, $b = 0.398$ nm, and $c = 1.16$ nm containing 20 atoms[38], has been utilized for DFT-based calculations of electronic properties. The larger supercell of the dimensions 1.18 nm × 1.19 nm × 1.13 nm, containing 60 atoms, was used to calculate the phonon properties of the Sb_2Se_3 crystal and its molecular dynamics. The dispersion of the phonon eigenvalues of Sb_2Se_3 crystal was calculated taking into account the van-der-Waals interaction in the form of the nonlocal vdW-DF functional optB86b-vdw[39].

Results and discussion

First principle calculations of electron and phonon properties of Sb_xSe_y films

The calculated dielectric permittivities ε_∞ (electronic contribution) and ε_{ion} (ionic contribution) of Sb_2Se_3 crystal (Table 2) are in acceptable agreement with the experimental ones presented in Ref[21]. To our knowledge, Ref[21]. provides a detailed experimental study of the reflection spectra and corresponding dielectric functions of Sb_2Se_3 single crystals in the far-infrared range, as well as a theoretical study of the phonon modes for the crystal at the orthorhombic space group of symmetry *Pnma* (no. 62).

In the present study, instead, the experimental reflection spectra of Sb_2Se_3 polycrystalline films deposited on soda-lime-glass substrates are measured in the far-infrared range. The stoichiometry and crystal structure of these polycrystalline films may differ from the corresponding features in the above-mentioned Sb_2Se_3 single crystals. Furthermore, first-principles calculations based on density functional theory of the Sb_2Se_3 single crystal were performed, taking into account the van der Waals interaction, and the corresponding dielectric function was obtained. The imaginary part of this dielectric function is used for comparison with the experimental reflection spectra of the studied Sb_2Se_3 films. The present study aims to provide more information on the electron and phonon properties of both stoichiometric and non-stoichiometric Sb_2Se_3 crystals, which may be utilized for the practical applications of Sb_2Se_3 films in solar cell technology.

According to the analysis of the accuracy of the experimental dielectric function curves ε(ν) performed in Ref[21]., the accuracy of determining the electronic dielectric permittivity ε_∞ was estimated to be about 20%, while the corresponding error for the ionic dielectric permittivity, $\Delta\varepsilon_{ion}/\varepsilon_{ion}$, can be larger. The relative differences between the averaged theoretical (row 5 of Table 2) and experimental (row 6 of Table 2) dielectric permittivities are presented in row 7 of Table 2. The obtained relative differences $2\times|\varepsilon_t - \varepsilon_e|/(\varepsilon_t + \varepsilon_e)$, appear acceptable when

Dielectric permittivity e.-and-c. functional	$\varepsilon_{\infty x}$	$\varepsilon_{\infty y}$	$\varepsilon_{\infty z}$	ε_{ion_x}	ε_{ion_y}	ε_{ion_z}
GGA-PE	9.71	18.7	18.3	3.27	63.4	80.8
GGA-PS	15.3	24.8	25.7	5.19	69.2	100
GGA-MK + vdW	13.7	22.8	23.8	4.40	69.0	111
Averaged theoretical ε_t	17.5		22.6	35.7		97.3
Experimental ε_e from Ref[21].	14.5		15.1	52		128
Relative difference $2\times\lvert\varepsilon_t - \varepsilon_e\rvert/(\varepsilon_t + \varepsilon_e)$	0.20		0.40	0.37		0.27

Table 2. Calculated cartesian components of the macroscopic static dielectric permittivities, ε_∞ (electronic contribution) and ε_{ion} (ionic contribution), of Sb_2Se_3 crystal at the space group of symmetry *Pnma* (no. 62) calculated for GGA-PE, GGA-PS, and GGA-MK + vdW exchange-and-correlation functionals.

considering that the theoretical and experimental accuracies of determining the dielectric permittivity are both approximately 20%. The characteristic feature of Sb_2Se_3 crystal is the large anisotropy of the calculated dielectric permittivity tensor ε: the contributions to the averaged dielectric permittivity from the *y*- and *z*-directions of the crystal are much larger than that from the *x*- one (Table 2). The spontaneous electric polarization in Sb_2Se_3 crystal and Sb_xSe_y deposited films is not expected because the space group of symmetry *Pnma* is nonpolar. The absence of polar symmetry in Sb_xSe_y films may be partly caused by the relatively small difference of antimony and selenium electronegativities, $\chi^{(Se)} - \chi^{(Sb)} = 0.5$ (Pauling scale), which corresponds to the relatively small ionic character (IC)[40] of Sb Se bonding, IC = %. Small ionic character of Sb Se bonds may cause small Sb Se dipole moments in Sb_xSe_y films, which can decrease the probability of polarized parts arising in these films during their deposition on a substrate.

It is known[13] that the interatomic bonding in Sb_2Se_3 crystal is strongly anisotropic because the covalently bonded $(Sb_4Se_6)_n$ ribbon-like structure elements are realized along one of the crystallographic directions ([001]) and weaker forces take place in the two other orthogonal directions. Very high anisotropy of the dielectric properties in Sb_2Se_3 is observed for the ionic part of the dielectric permittivity, $\varepsilon_{ion\_x} << \varepsilon_{ion\_y}$, $\varepsilon_{ion\_x} << \varepsilon_{ion\_z}$ (Table 2). Similar but not so high anisotropy of the dielectric properties in Sb_2Se_3 takes place for the electronic part of the dielectric permittivity, $\varepsilon_{\infty x} < \varepsilon_{\infty y}$, $\varepsilon_{\infty x} < \varepsilon_{\infty z}$ (Table 2). The observed anisotropy of the dielectric permittivity tensor corresponds to the layer-like crystal structure of Sb_2Se_3, for which the corresponding quasi-layers are perpendicular to the [100] direction (*a*-direction) (Fig. 5). Thus, the comparatively weak van-der-Waals interaction is realized between the quasi-layers with boundaries indicated in the *b*-cut view of Sb_2Se_3 crystal structure by the thick horizontal lines (Fig. 5). The relatively weak van-der-Waals interaction in [100] direction of the crystal is a reason for the much smaller ionic and smaller electronic parts of dielectric permittivity in this direction in comparison to [010] and [001] ones (Table 2). No layer-like crystal structure is found in the [010] direction (*b*-direction).

Dispersion of the phonon energy bands of Sb_2Se_3 crystal is observed in the frequency range of 0–220 cm^{-1}, where the acoustic modes are realized in the range of 0–50 cm^{-1} and the optical modes are observed in the range of 50–220 cm^{-1} (Fig. 6a, b). The phonon dispersions of Sb_2Se_3 calculated for PBE and PBEsol exchange-and-correlation functional are close to one another (Fig. 6a, b). Negative frequencies were observed in the dispersion dependence ν(*Q*), calculated without taking into account the vdW interaction and this happened in the *Q*-segments Γ X and Z – U, where the $Q_{[100]}$ component was changing. This result is caused by the relatively weak interatomic interaction in the [100] direction of the crystal (Fig. 5). Another manifestation of the relatively weak interatomic interaction in the [100] direction of the crystal is the flat dispersion dependences ν(*Q*) at the segments S – Y, Z – U, and R – T, where the changes of the type, $[0Q_yQ_z] \leftrightarrow [\frac{1}{2}Q_yQ_z]$, of the phonon *Q*-points in the Brillouin zone take place.

The calculated vibration total and partial densities of states (vDOS and vPDOS) of Sb_2Se_3 crystal (Fig. 7) are characterized by numerous maxima, which correspond to the numerous groups of phonon energy bands (Fig. 6). Clear hybridization of the antimony and selenium vibration states is observed, which is manifested by the equality of the frequency positions of $vPDOS^{(Sb)}$ and $vPDOS^{(Se)}$ maxima (Fig. 7b). The characteristic feature of these vPDOS is a dominance of the antimony density of states in the frequency range 0–90 cm^{-1} and a dominance of the selenium density of states in the range 90–190 cm^{-1} (Fig. 7b). The latter feature is expected because of the larger atomic mass of antimony atom ($M^{(Sb)} = 121.76$) in comparison to the mass of selenium one ($M^{(Sb)} = 78.971$).

The results of our DFT-based calculations of lattice dynamics of Sb_2Se_3 crystal have shown that the corresponding infrared phonon excitations take place in the frequency range of 50–220 cm^{-1}. According to these

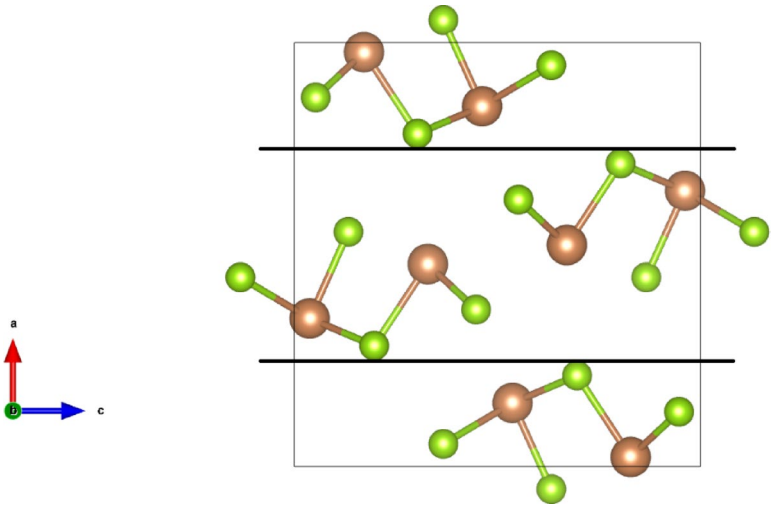

Fig. 5. The *b*-cut view of Sb_2Se_3 crystal structure at *Pnma* (no. 62) space group of symmetry. Thick horizontal lines indicate planes of boundaries between structural layers perpendicular to the *a*-axis of the crystal's unit cell.

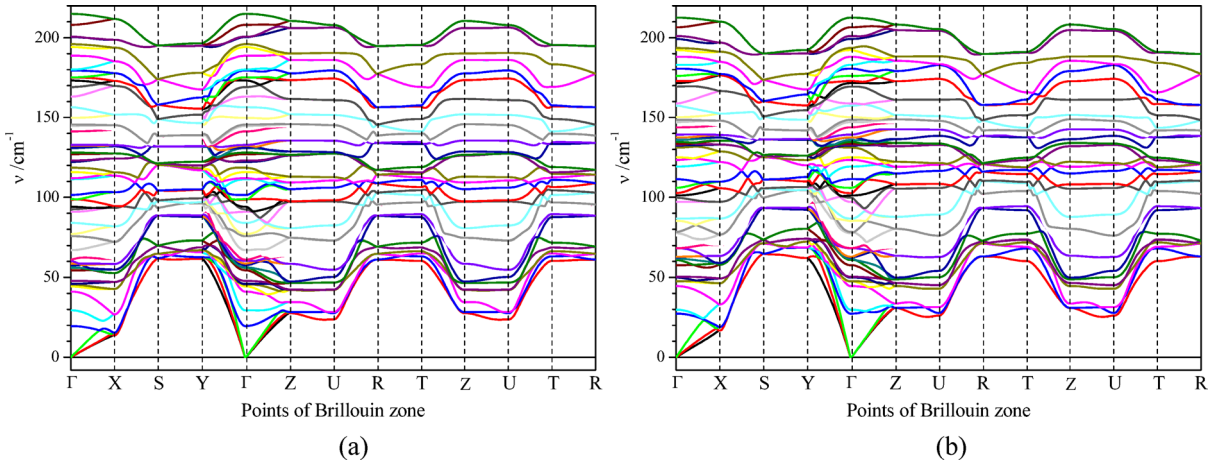

Fig. 6. Dispersions of phonon energy bands of Sb_2Se_3 calculated with using van-der-Waals interaction of DFT-D3 method of Grimme[41,42] at (a) PBE and (b) PBEsol exchange-and-correlation functionals. The correspondence of the Brillouin zone symbols and *Q*-points is following: Γ[000], X[$\frac{1}{2}$00], S[$\frac{1}{2}\frac{1}{2}$0], Y[0$\frac{1}{2}$0], Z[00$\frac{1}{2}$], U[$\frac{1}{2}$0$\frac{1}{2}$], R[$\frac{1}{2}\frac{1}{2}\frac{1}{2}$], T[0$\frac{1}{2}\frac{1}{2}$].

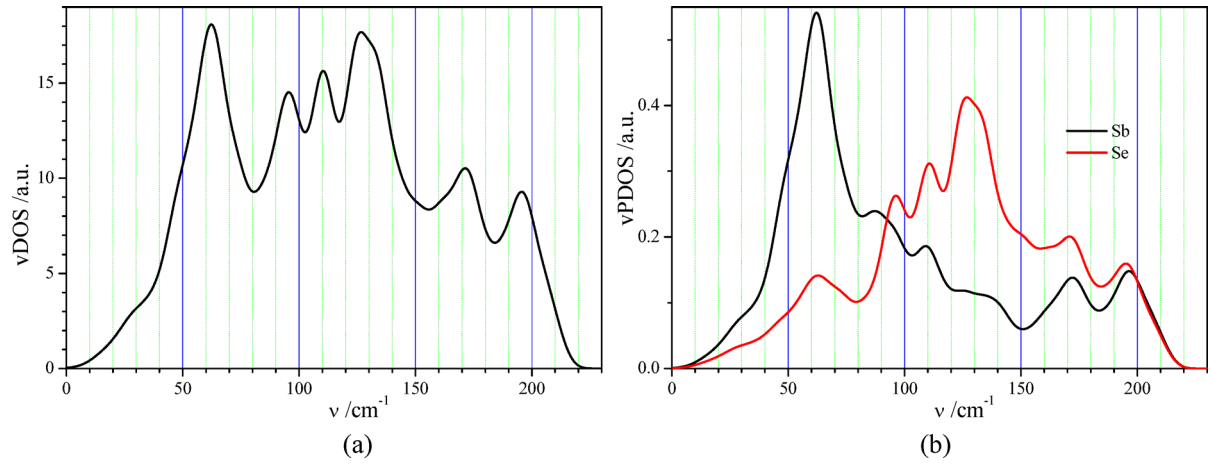

Fig. 7. (a) Vibration density of states vDOS and (b) vibration partial density of states vPDOS of antimony and selenium atoms in Sb_2Se_3 crystal calculated at PBE exchange-and-correlation functional.

results, the spectral range above 220 cm^{-1} should be the range of crystal transparency, if some other mechanisms of radiation absorption are absent. However, from the SEM and EDX results of the deposited films, we also expect the metallic phase of the redundant antimony, which can be the source of free electrons. These free electrons may cause the inverse proportional dependence of the reflection coefficient *R* on the frequency ν[43].

Reflection spectra in the far-infrared spectral range Sb_xSe_y films

Analysis of Sb_xSe_y reflection spectra $R(\nu)$ shows the presence of an interference-like structure in the frequency range of $\nu > 1200$ cm^{-1} for several samples (Fig. 8a). The distances between neighboring interference extrema for samples no. 3, 4, and 7 correspond to film thicknesses of about 1 μm, which are close to the values determined by the other method (Table 1). The absence of a clear interference-like structure for other films in Fig. 8a can be caused by the relatively strong radiation scattering on their rough surfaces. This suggestion is in agreement with the observed quasi-monotonous decrease of the reflection coefficient *R* with the increase of the frequency ν, caused by the surface roughness, which is expected for the mean surface roughness of about 0.5 μm (see the cross-sections of films in Fig. 1).

The reflection spectra $R(\nu)$ in the range $\nu < 230$ cm^{-1} are presented in Fig. 8b for Sb_xSe_y films studied. The largest reflection coefficients are observed for the samples 1, 2 and 5 (Fig. 8b). This is caused by the increased amount of metal phase of antimony in the deposited films and, consequently, by the increased reflection coefficients due to Drude-like behavior in the far-infrared range[43]. The mean value/level of the reflection coefficient of Sb_xSe_y films in the range of 25 230 cm^{-1} (Fig. 8b) is proportional to the concentration of residual antimony atoms (Fig. 2b), being in the metal-like state, compared to their bonded states in the Sb_2Se_3 polycrystals.

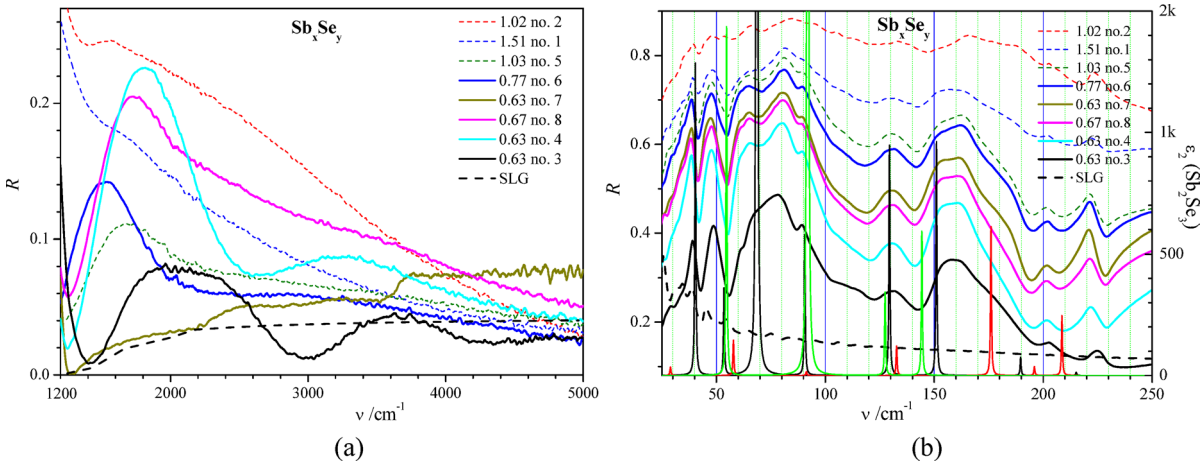

Fig. 8. (a) Reflection spectra $R(\nu)$ of eight Sb_xSe_y films on soda-lime glass substrates (SLG) and SLG measured at room temperature. The legend values correspond to the index of compound relation x/y determined from EDX measurements and sample number (Fig. 2b, d). The values of R correspond to the absolute reflection coefficients. The experimental calibration of the R scale was performed using the gold mirror and its known optical constants. (b) Reflection spectra $R(\nu)$ of eight Sb_xSe_y films on soda-lime glass substrates (SLG) and SLG measured at room temperature and theoretical spectra of imaginary part of dielectric permittivity $\varepsilon_2(\nu)$ (narrow black, red and green peaks). Here, for $\varepsilon_2(\nu)$ spectra, black, red and green colors correspond to the light polarizations along x-, y-, and z-axis of Sb_2Se_3 crystal at the space group of symmetry *Pnma* (no. 62). The legend values correspond to the index of compound relation x/y determined from EDX measurements and sample number (Fig. 2b, d). The values of R correspond to the absolute reflection coefficients. The experimental calibration of the R scale was performed using the gold mirror and its known optical constants.

The reflection spectra of Sb_xSe_y films in the far-IR range are similar because of the almost identical positions of $R(\nu)$ peaks (Fig. 8b). The highest similarity is observed for the spectra of samples 4–8, which may confirm the formation of the same crystalline phase Sb_2Se_3 in these samples. These positions are in good quantitative agreement with the positions of maxima of the imaginary part of the dielectric function $\varepsilon_2(\nu)$ obtained from our first-principle calculations of Sb_2Se_3 crystal within the framework of DFT (Fig. 8b). The structure of the reflection spectra $R(\nu)$ measured for Sb_xSe_y films (Fig. 8b) is rather similar to that obtained experimentally for Sb_2Se_3 single crystals[21]. The latter was also observed in a similar spectral range, 25–210 cm^{-1}, and was characterized by a similar number of reflection maxima. One of the clear differences between the experimental reflection spectra of the Sb_2Se_3 films studied (Fig. 8b) and the reflection spectrum of an Sb_2Se_3 single crystal is the reflection maximum in Sb_2Se_3 films in the range 221–225 cm^{-1} (Fig. 8b), which is absent in this frequency range in Sb_2Se_3 single crystal[21]. This should be caused by the vibration mode associated with the special states of selenium ions in Sb_2Se_3 films, which are absent in the corresponding single crystal. This should be associated with the selenium ions, first of all, because the vibration states of selenium ions are characterized by a larger vPDOS compared to the vPDOS of antimony ones in the high-frequency part of the Sb_2Se_3 phonon spectrum (Fig. 8b). Such special vibration states of the selenium ions may be the states of Se – Sb bonds created on the surface of Sb_2Se_3 nanocrystals in Sb_xSe_y films. The corresponding frequency shifts of the Raman-active and the IR-active modes for sized and layered two-dimensional structures were observed in different nanomaterials[44–48]. The reflection maximum in Sb_2Se_3 films in the range 221–225 cm^{-1} (Fig. 8b) may originate, in principle, from the Se – Se vibrations of the defect structure of Sb_xSe_y films studied. This possibility is mentioned in Ref[49]. (see the selected Raman frequencies in Table 3). On the basis of the experimental reflection spectra obtained in the far-IR range for eight Sb_xSe_y films (Fig. 8b), we tried to study the correlation between the relative value of the reflection maximum, R_{max} - R_{min}, in the range 221–225 cm^{-1} (Fig. 8b) and the relation $c(Se)/c(Sb)$ of the concentrations of selenium and antimony atoms (see Fig. 3c). We have found a weak positive correlation of these values (Fig. 9a), which supports the statement of the prevalent selenium origin of the reflection maximum in the frequency range 221–225 cm^{-1}.

We have calculated the Raman spectrum of the Sb_2Se_3 crystal at the space group symmetry of *Pnma* (No. 62) (Fig. 9b) using CASTEP code[50] and have found that it is very similar to the experimental Raman spectra obtained for Sb_2Se_3 films deposited by the same method (CMBD) on the same substrates (soda-lime glass) by several authors of the present study Ref[49]. Besides, the calculated frequency positions of the Raman spectrum of Sb_2Se_3 crystal (Fig. 9b) agree satisfactorily with the corresponding experimental Raman spectrum[51] and with Raman spectra of Sb_2Se_3 films[52].

Discussion

The increased reflection coefficients of Sb_xSe_y films for several x/y relations in the wide spectral range 30–5000 cm^{-1} (Fig. 8) may be caused by the over-stoichiometric antimony content, leading to the metal-like character of the radiation reflection. To verify this supposition we have performed DFT calculations of the electron energy structure of the contents $Sb_{25}Se_{36}$ and $Sb_{26}Se_{36}$, which contain one ($Sb_{25}Se_{36}$) and two ($Sb_{26}Se_{36}$)

830	840	900	975	980	1000	Sb	Se_n, spiral chains	Se_6, red selen (rings)	Sb_2O_3
80	85	80	80	80	77				
101	102	99	102	102	72			102	
117	110	110	118	110	110	110			
					118				118
123	122	123	123	129	125				123
			129		131			129	
				139	139				140
153	153	153	153	153	153	151			
190	190	190	188	185	187				189
208	212	208	212	209	209				
233	235		238	235			**234–237**		
			251	254	257			**250**	**255**

Table 3. Peak positions of Raman modes (in cm^{-1}) of Sb_xSe_y films deposited at different source temperatures in the range 830–1000 °C and Raman modes of different crystalline substances containing Sb and se atoms[49].

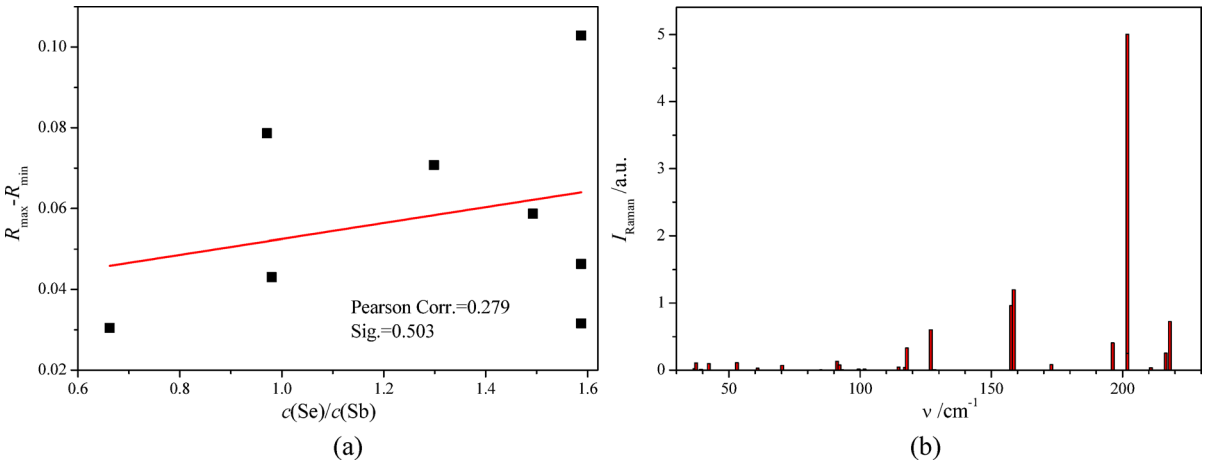

Fig. 9. (a) Dependence of the relative value of the reflection maximum, R_{max} - R_{min}, in the range 221–225 cm^{-1} (see Fig. 8b) and the relation of the concentrations of selenium and antimony atoms c(Se)/c(Sb), (see Fig. 3c). The red direct line is the linear fit of this dependence. (b) Raman spectrum $I_{Raman}(\nu)$ of Sb_2Se_3 crystal at the space group symmetry of *Pnma* (No. 62) calculated using CASTEP code at PBEsol exchange-and-correlation functional.

residual antimony atoms in the $1 \times 3 \times 1$ supercell of the elementary unit cell of Sb_8Se_{12}. The optimized positions of these residual antimony atoms Sb1 and Sb2 are shown in Fig. 10.

For the calculations of the density of states and bandgap E_g of the crystals $Sb_{24}Se_{36}$, $Sb_{25}Se_{36}$, and $Sb_{26}Se_{36}$, we have utilized the HSEsol hybrid exchange-and-correlation functional[53], which is often used for the calculations of the energy bandgap E_g of crystals with high reliability. The obtained bandgap of the stoichiometric crystal $Sb_{24}Se_{36}$ is found to be E_g = 1.28 eV. In the calculated density of states of the content $Sb_{25}Se_{36}$, one separate maximum of the valence states is at the energy of 4.8 eV, which is below the Fermi level of the crystal E_F = 5.414 eV (Fig. 11a). The maximum of the partial density of states of $Sb_{25}Se_{36}$ at 4.8 eV (Fig. 11b) is formed mainly by the electronic states of the residual antimony ion. In the over-stoichiometric content $Sb_{25}Se_{36}$, the bandgap is smaller, E_g = 0.923 eV, and numerous partly-occupied electronic states are in the upper part of the forbidden energy gap (Fig. 12). The electron states at the Fermi energy, $E \geq E_F$, and the thermally stimulated transitions of electrons from the upper donor energy states of the residual antimony atoms to the conduction band of $Sb_{25}Se_{36}$ can form a free electron plasma. This plasma increases the optical reflection coefficient of the $Sb_{25}Se_{36}$ layer in the range of 25–250 cm^{-1} (Fig. 8b) according to the Drude relation[43]. The electron states just below the Fermi level E_F (Fig. 12) may also be excited by photons to the lowest states of the conduction band (Fig. 11), thus forming the infrared absorption spectrum in the photon energy range of 1200–5000 cm^{-1} (0.15–0.62 eV).

The optical bandgap E_g of Sb_xSe_y films of thickness d was determined from the measurements of their transmittance T as a function of the photon energy $h\nu$ (Fig. SD-9 of Supplementary designation). The bandgap E_g was obtained from the slope of the linear part of the dependence of the value $(-h\nu \cdot \ln(T)/d)^2$ on the photon energy $h\nu$, corresponding to the direct optical transitions. It was found that the dependence of the bandgap E_g of Sb_xSe_y films on their content index x/y ($x/y = N_{Sb}/N_{Se}$) is close to a linear one with a negative slope coefficient

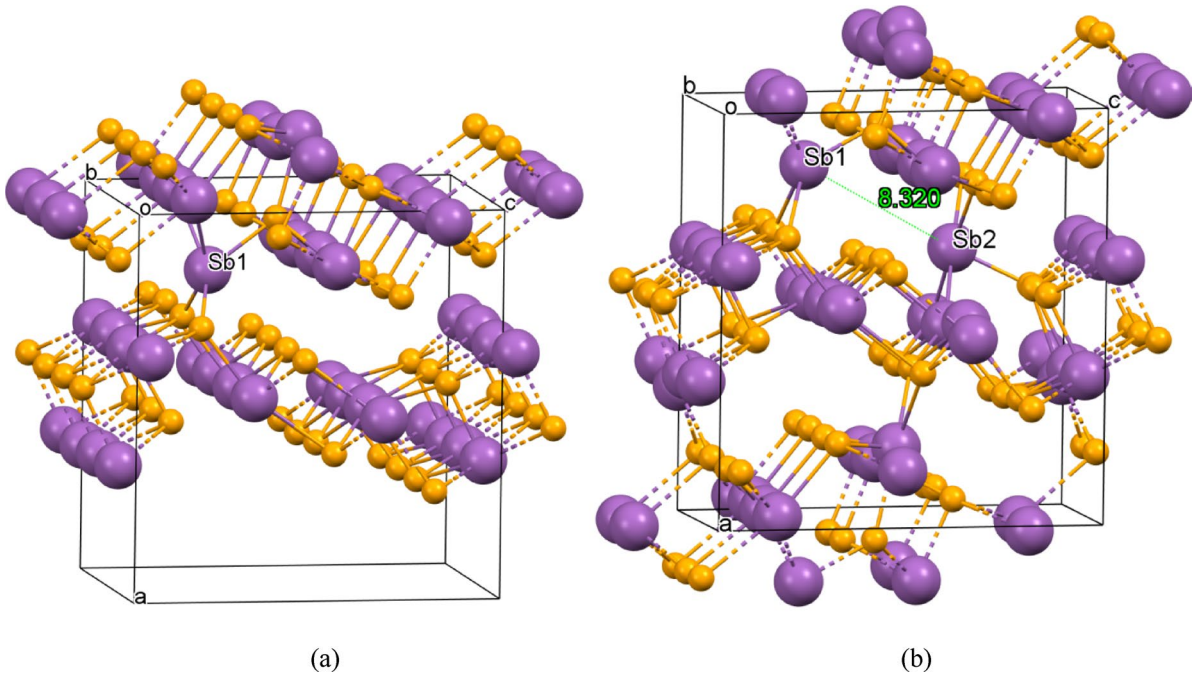

Fig. 10. Positions of the residual antimony atoms Sb1 and Sb2 in the over-stoichiometric contents $Sb_{25}Se_{36}$ (a) and $Sb_{26}Se_{36}$ (b) corresponding to the supercell $1 \times 3 \times 1$ of the elementary unit cell $1 \times 1 \times 1$ (Sb_8Se_{12}). The distance $d = 8.32$ Å between two residual antimony atoms is indicated in the part (b) of the figure.

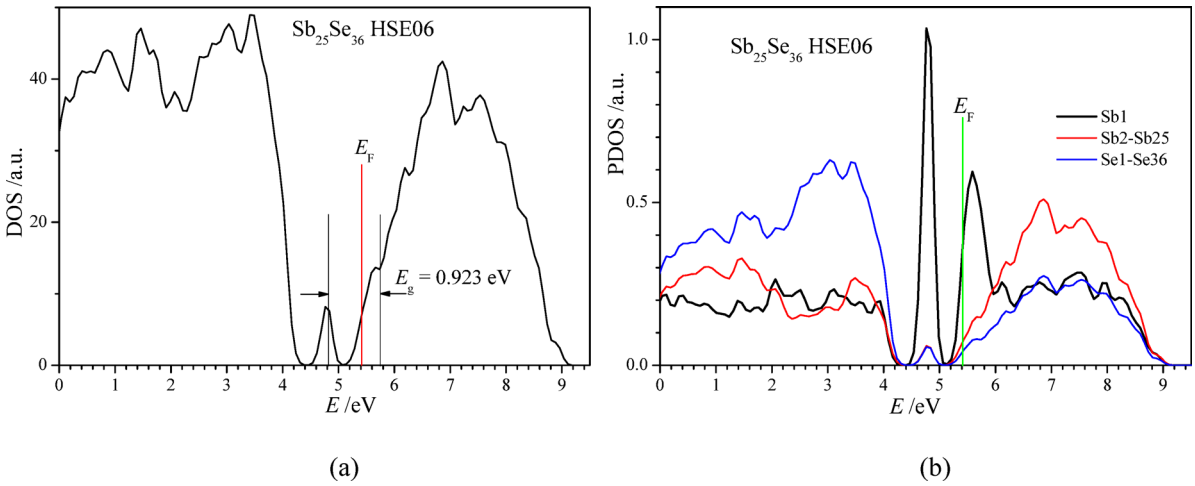

Fig. 11. Calculated density of states (a) and partial density of states (b) of antimony selenide $Sb_{25}Se_{36}$ with one additional antimony atom in $1 \times 3 \times 1$ supercell ($Sb_{24}Se_{36}$) of the elementary unit cell (Sb_8Se_{12}) of Sb_2Se_3.

$dE_g/d(x/y)$ and is similar to that obtained in the previous study[54] (Fig. 13a). However, the absolute value of the experimental slope coefficient $|dE_g/d(x/y)| = 0.292$ (Fig. 13a) is substantially smaller than the theoretical one $|dE_g/d(x/y)| = 10.07$ (13b). This is likely caused by the fact that the majority of the residual antimony atoms are placed out of the polycrystals of Sb_xSe_y films in the form of a metallic phase in Sb_xSe_y films as already seen by XRD analysis. The latter circumstance also explains the experimentally observed increase of the reflection coefficient of Sb_xSe_y films with an increase of the N_{Sb}/N_{Se} relation (Fig. 8).

To confirm the supposition that the majority of the non-stoichiometric antimony atoms can be aggregated outside the polycrystals Sb_2Se_3 in Sb_xSe_y films we have performed comparative calculations of the total energy of (a) one and two residual antimony atoms inside $Sb_{24}Se_{36}$ supercell and (b) one residual antimony atom adsorbed on the surface of $Sb_{48}Se_{72}$ supercell. In the latter case, a twice larger supercell dimension perpendicular to the surfaces of the $Sb_{48}Se_{72}$ slab was chosen to minimize the atomic interaction between atoms of two parallel slabs' surfaces. For the residual antimony atom localized inside the $Sb_{24}Se_{36}$ supercell, the binding energy $E_b^{(Sb)}$ ranges from 3.10 to 3.51 eV (Table 4). For the non-stoichiometric antimony atom localized on the slab's surfaces [100],

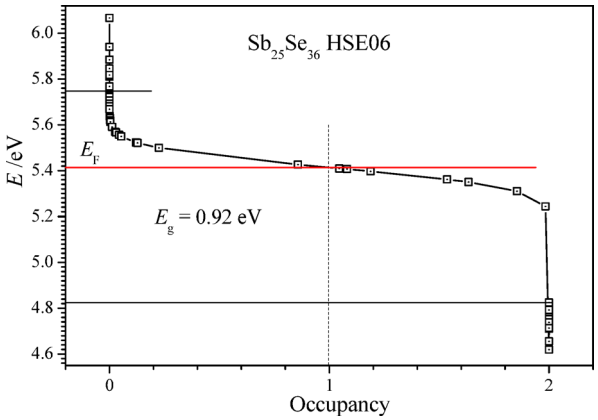

Fig. 12. Energy of electron states E, in the range of the bandgap E_g, versus their electron occupancy calculated for non-stoichiometric $Sb_{25}Se_{36}$ ($Sb + Sb_{24}Se_{36}$) with one additional antimony atom in $1 \times 3 \times 1$ supercell ($Sb_{24}Se_{36}$) of the elementary unit cell (Sb_8Se_{12}) of Sb_2Se_3.

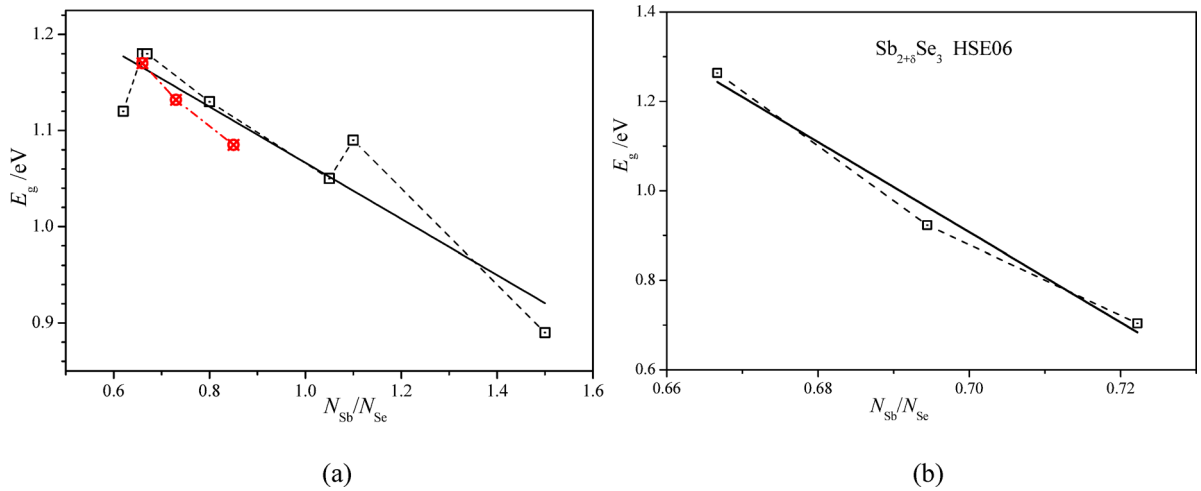

Fig. 13. Dependences (a) of the optical bandgap E_g of Sb_xSe_y films determined by the transmittance measurements $T(h\nu)$ (red points relate to the corresponding experimental study in Ref[54]. and (b) of the theoretical optical bandgap E_g of $Sb_{24}Se_{36}$, $Sb_{25}Se_{36}$, and $Sb_{26}Se_{36}$ crystals on their atomic content N_{Sb}/N_{Se}.

Supercell content	i	E /eV	$E_b^{(Sb)}$ eV
$Sb_{24}Se_{36}$	0	−312.195	-
$Sb_{25}Se_{36}$	1	−315.300	3.10
$Sb_{26}Se_{36}$	2	−319.223	3.51

Table 4. Total energy E for supercell contents $Sb_{24}Se_{36}$, $Sb_{25}Se_{36}$, and $Sb_{26}Se_{36}$ and binding energy $E_b^{(Sb)}$ for the residual antimony atom in $Sb_{25}Se_{36}$ and $Sb_{26}Se_{36}$ supercells.

[010], and [001] originated from the $Sb_{48}Se_{72}$ supercell, the binding energy $E_b^{(Sb)}$ is found to be in the range of 3.35 4.19 eV (Table 5). These results indicate that the probability of localization of the non-stoichiometric antimony atoms on the [100], [010], and [001] facets of the polycrystals Sb_2Se_3 in Sb_xSe_y films is greater than that inside these polycrystals.

On the other hand, we have found that the calculated cohesive (or binding) energies of the metallic antimony (Sb) and antimony selenide (Sb_2Se_3) crystals are respectively equal to $E_c^{(Sb)} = 3.12$ eV and $E_c^{(Sb2Se3)} = 3.34$ eV. This, in turn, indicates that the probability of crystal growth of Sb_2Se_3 is higher than that of the metallic antimony. These results indicate that during Sb_xSe_y film deposition, the growth of Sb_2Se_3 crystals is preferable to the independent growth of metallic antimony crystals. However, the growth of metallic antimony crystals becomes more probable on the surfaces of Sb_2Se_3 crystals due to the high bonding energy of the antimony

One Sb on $Sb_{24}Se_{36}$ slab	E/eV	$E_b^{(Sb)}$/eV
$Sb_{24}Se_{36}$ slab [100]	−519.825	-
$Sb_{24}Se_{36}$ slab [100] + Sb	−524.018	4.19
$Sb_{24}Se_{36}$ slab [010]	−521.232	-
$Sb_{24}Se_{36}$ slab [010] + Sb	−525.125	3.89
$Sb_{24}Se_{36}$ slab [001]	−521.576	-
$Sb_{24}Se_{36}$ slab [001] + Sb	−524.932	3.35

Table 5. Total energy E of $Sb_{24}Se_{36}$ slabs [100], [010], and [001] and one antimony atom on the surfaces of these slabs and binding energy of the residual antimony atom $E_b^{(Sb)}$ on the surfaces of these slabs.

atoms $E_b^{(Sb)}$ on the facets of Sb_2Se_3 crystals (Table 5). Moreover, in the late stages of Sb_xSe_y film deposition, the over-stoichiometric antimony atoms of Sb_2Se_3 crystals can move due to diffusion from the inner parts of the Sb_2Se_3 crystal to its surface, because of the larger binding energy of the antimony atoms on the crystal facets (3.35–4.19 eV, Table 5) in comparison to its body (3.10–3.51 eV, Table 4). These factors may promote the possibility of depositing the over-stoichiometric antimony on the facets of Sb_2Se_3 polycrystals in the form of a thin metallic antimony layer. In turn, such a metallic antimony layer on Sb_xSe_y films studied may be a reason for the increasing reflection coefficient in the far-infrared range with increasing their antimony content due to the free electron plasma (Fig. 8b). The proposed explanation agrees with the XRD measurements of the films studied (see Chap. 2), in which two main substances, the antimony selenide Sb_2Se_3 and the residual metallic Sb, were detected.

Summarizing the results obtained for Sb_2Se_3-based films, one can state that the experimental and theoretical studies of the optical properties of the films in the wide infrared range of 30–8000 cm^{-1} can be useful for checking the necessary properties important for the photoelectric applications of these and similar semiconductor films.

In the spectral range of 500–8000 cm^{-1} (0.06–0.99 eV), one can obtain information mainly on the possible local and distributed electron states caused by doping and structural imperfections in the films deposited by different methods. The local electron states can be detected in the form of spectral bands, which are frequently observed at relatively low temperatures. In turn, the distributed electron states are revealed as quasi-free electrons or holes, which can be fitted by the known Drude-Lorentz relation[43]. In the studied Sb_2Se_3-based films, both types of electron states occur. The local electron states in these films can cause the dependence of their bandgap Eg on the antimony content (Fig. 13). In turn, the quasi-free electrons or holes in the films are revealed in the increased level of the reflection coefficient for the frequencies, which are proportional to the concentration of these carriers (Fig. 8b).

In the spectral range of 30–240 cm^{-1} (3.72–30 meV), phonon excitations in Sb_2Se_3-based films are revealed in the form of well-defined spectral peaks (Fig. 8b). The phonon spectral structure is closely related to the spatial symmetry and interatomic distances in the Sb_2Se_3 polycrystals that form the deposited films. Thus, these characteristics, when obtained for the deposited Sb_2Se_3-based films, may also be useful for the optimization of the corresponding deposition conditions.

Conclusions

It was confirmed that it is possible to obtain stoichiometric Sb_2Se_3 layers using the molecular beam chemical deposition method by applying optimal deposition conditions. The EDX and XRD analysis showed that most of the films investigated in current studies contain excess antimony in various concentrations. Therefore, they provide an optimal basis for studying the effect of excess antimony on the electron and phonon properties of Sb_xSe_y films, which ultimately determines their usefulness in photovoltaics.

The experimental and theoretical dependences of the bandgap E_g on the concentration of residual antimony atoms in the Sb_xSe_y films, in relation to Sb_2Se_3 crystals, have been obtained, which can be useful for the photovoltaic application of these films.

The structure of the phonon reflection spectra of Sb_xSe_y films for different relations x/y of the deposited Sb_xSe_y films are similar, while the averaged reflection coefficient is proportional to the relation x/y. The positions of the measured reflection maxima of Sb_xSe_y thick films agree with the calculated frequency positions of the imaginary part of the dielectric function $\varepsilon_2(\nu)$ of Sb_2Se_3 single crystal in Ref[21]. The latter result confirms that the main crystal compound Sb_2Se_3 remains unchanged for different relations x/y in Sb_xSe_y thick films.

The mean value/level of the reflection coefficient of Sb_xSe_y films in the range of 25 230 cm^{-1} is found to be proportional to the residual concentration of the antimony atoms, being in the metal-like state, compared to their bonded states in Sb_2Se_3 compound. This further confirms the presence of metallic antimony in the Sb_xSe_y films studied. The present findings are further supported by experimental and theoretical studies of the optical bandgap E_g of Sb_xSe_y films and $Sb_{24+i}Se_{36}$ ($i = 0, 1, 2$) crystals and the expected change of bandgap E_g with an increase of the relative concentration of the residual antimony atoms (N_{Sb}/N_{Se}). Comparison of these experimental and theoretical dependences $E_g(N_{Sb}/N_{Se})$ revealed that only a limited part of the residual antimony atoms can stay inside the Sb_2Se_3 matrix, and the rest of the residual antimony atoms could, in principle, migrate to the surface of Sb_2Se_3 grains, creating the metallic antimony phase.

For the residual antimony atoms localized inside the $Sb_{24}Se_{36}$ supercell, the binding energy $E_b^{(Sb)}$ (3.10 3.51 eV) is smaller than that corresponding to the antimony atoms adsorbed on the surfaces of Sb_2Se_3 polycrystals (3.35 4.19 eV). This should lead to the thermal diffusion of the antimony atoms from the body to the facets of Sb_2Se_3

polycrystals and the formation of a metallic antimony thin film. This finding confirms the supposition that the majority of the non-stoichiometric antimony atoms can aggregate outside the polycrystals Sb_2Se_3 in Sb_xSe_y films in the form of the metallic antimony thin film. This thin metallic surface film should increase the reflection coefficient of Sb_xSe_y films studied in the far-infrared range due to the known free electron plasma effect.

Data availability

The datasets generated and/or analysed during the current study are not publicly available because the necessary datasets are presented in the manuscript, but the additional datasets of the study are available from the corresponding author on reasonable request.

Received: 31 May 2025; Accepted: 25 August 2025
Published online: 29 September 2025

References

1. Caño, I. et al. Does Sb_2Se_3 admit nonstoichiometric conditions? How modifying the overall se content affects the structural, optical, and optoelectronic properties of Sb_2Se_3 thin films. *ACS Appl. Mater. Interfaces*. **14**, 11222–11234 (2022).
2. Chen, C. et al. Optical properties of amorphous and polycrystalline Sb_2Se_3 thin films prepared by thermal evaporation. *Appl. Phys. Lett.* **107**, 043905 (2015).
3. Green, M. A. et al. Solar cell efficiency tables (Version 63). *Prog Photovolt. Res. Appl.* **32**, 3–13 (2024).
4. Masuko, K. et al. Achievement of more than 25% conversion efficiency with crystalline silicon heterojunction solar cell. *IEEE J. Photovolt.* **4**, 1433–1435 (2014).
5. Green, M. A. et al. Solar cell efficiency tables (version 56). *Prog Photovolt. Res. Appl.* **28**, 629–638 (2020).
6. Zhou, Y. et al. Solution-processed antimony Selenide heterojunction solar cells. *Adv. Energy Mater.* **4**, 1301846 (2014).
7. Cifuentes, N. et al. Electronic conduction mechanisms and defects in polycrystalline antimony Selenide. *J. Phys. Chem. C.* **124**, 7677–7682 (2020).
8. Yang, W. et al. Benchmark performance of low-cost Sb_2Se_3 photocathodes for unassisted solar overall water splitting. *Nat. Commun.* **11**, 861. https://doi.org/10.1038/s41467-020-14704-3 (2020).
9. Jayswal, N. K. et al. Optical properties of thin film Sb_2Se_3 and identification of its electronic losses in photovoltaic devices. *Sol. Energy*. **228**, 38–44 (2021).
10. Cai, Z. et al. Sb_2Se_3 as a bottom cell material for efficient perovskite/Sb_2Se_3 tandem solar cells. *Energy Mater. Devices*. **2** (1), 9370027 (2024).
11. Zhou, Y. et al. Thin-film Sb_2Se_3 photovoltaics with oriented one-dimensional ribbons and benign grain boundaries. *Nat. Photonics*. **9**, 409–415 (2015).
12. Ghosh, S., Moreira, M. V. B., Fantini, C. & González, J. C. Growth and optical properties of nanocrystalline Sb_2Se_3 thin-films for the application in solar-cells. *Sol. Energy*. **211**, 613–621 (2020).
13. Mavlonov, A. et al. Qiao, L. A review of Sb_2Se_3 photovoltaic absorber materials and thin-film solar cells. *Sol Energy*. **201**, 227–246 (2020).
14. Mavlonov, A. et al. Structural and morphological properties of PLD Sb_2Se_3 thin films for use in solar cells. *Sol. Energy*. **208**, 451–445 (2020).
15. Chen, C. et al. Characterization of basic physical properties of Sb_2Se_3 and its relevance for photovoltaics. *Front. Optoelectron.* **10**, 18–30 (2017).
16. Razykov, T. M. et al. Conductivity of Sb_xSe_y films grown by CMBD from Sb and se precursors for use in solar cells. *Sol. Energy*. **230**, 10–12 (2021).
17. Wijesinghe, U., Longo, G. & Hutter, O. S. Defect engineering in antimony Selenide thin film solar cells. *Energy Adv.* **2**, 12–33 (2023).
18. Huang, M., Xu, P., Han, D., Tang, J. & Chen, S. Complicated and unconventional defect properties of the quasi-one-dimensional photovoltaic semiconductor Sb_2Se_3. *ACS Appl. Mater. Interfaces*. **11**, 15564–15572 (2019).
19. Ghosha, S. et al. do, A. Comprehensive structural and surface investigation of Sb_2Se_3 thin-films. *Surf. Interfaces* **44**, 103693 (2024).
20. Maghraoui-Meherzia, H., Nasrb, B. & Dachraouia, T. Synthesis, structure and optical properties of Sb_2Se_3. *Mater. Sci. Semicond. Process.* **16**, 179–184 (2013).
21. Petzelt, J. & Grigas, J. Far infrared dielectric dispersion in Sb_2S_3, Bi_2S_3 and Sb_2Se_3 single crystals. *Ferroelectrics* **5**, 59–68 (1973).
22. Hromadko, L. et al. Physico-chemical properties of the thin films of the SbxSe100 − x system (x = 90, 85, 80). *Thin Solid Films* **569**, 17 (2014).
23. Koc, H., Mamedov, A. M., Deligoz, E. & Ozisik, H. First principles prediction of the elastic, electronic, and optical properties of Sb2S3 and Sb2Se3 compounds. *Solid State Sci.* **14**(8), 1211 (2012).
24. El-Wahabb, E. A., Fouad, S. S. & Fadel, M. J. Theoretical and experimental study of the conduction mechanism in Sb2 Se3 alloy. *Mater. Sci.* **38**(3), 527 (2003).
25. Mamta, Singh, Y., Maurya, K. K. & Singh, V. N. A review on properties, applications, and deposition techniques of antimony Selenide. *Sol Energy Mater. Sol Cells*. **230**, 111223 (2021).
26. Aubry, E., Lambert, J., Demange, V. & Billard, A. Effect of Na diffusion from glass substrate on the microstructural and photocatalytic properties of post-annealed TiO_2 films synthesised by reactive sputtering. *Surf. Coat. Technol.* **206**, 4999–5005 (2012).
27. Rudmann, D. et al. Tiwari, A. N. Sodium incorporation strategies for CIGS growth at different temperatures. *Thin Solid Films*. **480–481**, 55–60 (2005).
28. Schade, U., Ortolani, M. & Lee, J. THz experiments with coherent synchrotron radiation from BESSY II. *Synchrotron Radiation News*. **20**, 17–24 (2007).
29. Rubin, M. Optical properties of soda lime silica glasses. *Sol Energy Mater.* **12**, 275–288 (1985).
30. Kresse, G. & Hafner, J. Ab initio molecular dynamics for liquid metals. *Phys. Rev.* **B47**, 558–561 (1993).
31. Kresse, G. & Hafner, J. Ab initio molecular-dynamics simulation of the liquid-metal-amorphous-semiconductor transition in germanium. *Phys. Rev.* **B49**, 114251–114269 (1994).
32. Kresse, G. & Furthmüller, J. Efficiency of ab-initio total energy calculations for metals and semiconductors using a plane-wave basis set. *Comput. Mater. Sci.* **6**, 15–50 (1996).
33. Kresse, G. & Furthmüller, J. Efficient iterative schemes for Ab initio total-energy calculations using a plane-wave basis set. *Phys. Rev.* **B54**, 11169–11186 (1996).
34. Blöchl, P. E. Projector augmented-wave method. *Phys. Rev.* **B50**, 17953–17979 (1994).
35. Kresse, G. & Joubert, D. From ultrasoft pseudopotentials to the projector augmented-wave method. *Phys. Rev.* **B59**, 1758–1775 (1999).
36. Perdew, J. P. et al. Restoring the density-gradient expansion for exchange in solids and surfaces. *Phys. Rev. Lett.* **100**, 136406 (2008).
37. Methfessel, M. & Paxton, A. T. High-precision sampling for Brillouin-zone integration in metals. *Phys. Rev.* **B40**, 3616–3621 (1989).

38. Voutsas, G. P., Papazoglou, A. G. & Rentzeperi, P. J. The crystal structure of antimony Selenide Sb_2Se_3. *Z. Für Kristallographie*. **171**, 261–268 (1985).
39. Grimme, S. Semiempirical GGA-type density functional constructed with a long-range dispersion correction. *J. Comput. Chem.* **27**, 1787 (2006).
40. Callister, W. D. & Rethwisch, D. G. Jr. *Materials Science and Engineering: An Introduction* 43 (Wiley, 2014).
41. Grimme, S., Antony, J., Ehrlich, S. & Krieg, S. A consistent and accurate ab initio parametrization of density functional dispersion correction (DFT-D) for the 94 elements H-Pu. *J. Chem. Phys.* **132**, 154104 (2010).
42. Grimme, S., Ehrlich, S. & Goerigk, L. Effect of the damping function in dispersion corrected density functional theory. *J. Comput. Chem.* **32**, 1456 (2011).
43. Yu, P. Y. & Cardona, M. *Fundamentals of Semiconductors* 310 (Springer, 2010).
44. Zi, J. et al. Raman shifts in Si nanocrystals. *Appl. Phys. Lett.* **69** (2), 200–202 (1996).
45. Yang, X. X. et al. Raman spectroscopic determination of the length, strength, compressi4bility, Debye temperature, elasticity, and force constant of the C-C bond in graphene. *Nanoscale* **4** (2), 502–510 (2012).
46. Fujii, M., Kanzawa, Y., Hayashi, S. & Yamamoto, K. Raman scattering from acoustic phonons confined in Si nanocrystals. *Phys Rev. B* **54**(12), R8373–R8376 (1996).
47. Cheng, W. & Ren, S. F. Calculations on the size effects of Raman intensities of silicon quantum Dots. *Phys. Rev. B*. **65** (20), 205305 (2002).
48. Lee, C. et al. Anomalous lattice vibrations of single and few-layer MoS_2. *ACS Nano*. **4** (5), 2695–2700 (2010).
49. Razykov, T. M. et al. Characteristics of thin Sb_2Se_3 films obtained by the chemical molecular beam deposition method for thin-film solar cells. *Thin Solid Films*. **774**, 139844 (2023).
50. Clark, S. J. et al. First principles methods using CASTEP, zeitschrift fur kristallographie -. *Crystalline Mater.* **220**, 567–570 (2005).
51. Vidal-Fuentes, P. et al. Izquierdo roca. V. Multiwavelength excitation Raman scattering study of Sb_2Se_3 compound: fundamental vibrational properties and secondary phases detection. *2D Mater.* **6**, 045054 (2019).
52. Shongalova, A. et al. On the identification of Sb_2Se_3 using Raman scattering. *MRS Commun.* https://doi.org/10.1557/mrc.2018.94
53. Schimka, L., Harl, J. & Kresse, G. Improved hybrid functional for solids: the HSEsol functional. *J. Chem. Phys.* **134**, 024116 (2011).
54. Razykov, T. M. et al. Structural and optical properties of Sb_xSe_y thin films obtained by chemical molecular beam deposition method from Sb and se precursors. *Sol Energy*. **254**, 67–72 (2023).

Acknowledgements

This work was supported by the basic research program of the Academy of Sciences of the Republic of Uzbekistan. Experimental measurements using the synchrotron radiation of BESSY II operated by the Helmholtz-Zentrum Berlin für Materialien und Energie GmbH were performed in the framework of the BESSY proposal Project_222-11592-ST. Both the CoreLab CCMS and X-ray CoreLab at Helmholtz-Zentrum Berlin were used for measurements. Computer calculations were performed at ICM of Warsaw University, Poland (projects No. 89-1293, g93-1636, and g96-1832) and WCSS of the Wrocław University of Technology, Poland (project No. 053).

Author contributions

B. A. performed measurements of the infrared spectra and computer calculations of the material studied and wrote the manuscript. He is the corresponding author of the paper.L. (B) measured the infrared spectra of the material studied and elaborated on the corresponding experimental results. He participated in the discussion of the manuscript.A. P. prepared the necessary data for the computer calculations of the material studied and discussed the initial version of the manuscript.T. R. is the chief of the works on the deposition of Sb2Se3 thin films and measuring their characteristics. He prepared the corresponding parts of the manuscript.B. E. took part in the deposition of Sb2Se3 thin films and measured their characteristics. He prepared the corresponding chapters of the manuscript.K. K. took part in the deposition of Sb2Se3 and the preparation of the corresponding chapters of the manuscript.R. K. took part in the deposition of Sb2Se3 and the preparation of the corresponding chapters of the manuscript.D. I. took part in the measurements of Sb2Se3 thin film characteristics.M. P. took part in the measurements of Sb2Se3 thin film characteristics.U. S. took part in the measurements of the infrared spectra of the material studied and prepared the corresponding chapters of the manuscript.F. R. performed measurements of the thin films studied using SEM, EDX and XRD methods and wrote the corresponding chapters of the manuscript.A. S. performed measurements of the thin films studied using XRD method and prepared the corresponding part of the manuscript.R. S. performed measurements of the thin films studied using XRD method and prepared the corresponding part of the manuscript.L. P. took part in the measurements of the infrared spectra of the material studied and prepared the corresponding chapters of the manuscript.A. V. took part in the measurements of the infrared spectra of the material studied and discussed the initial version of the manuscript.A. K. performed the computer calculations of the electronic properties of the materials studied and prepared the corresponding part of the manuscript.M. P. performed the computer calculations of the Raman spectra of the material studied and participated in the preparation of the text of manuscript.

Declarations

Competing interests

The authors declare no competing interests.

Additional information

Supplementary Information The online version contains supplementary material available at https://doi.org/10.1038/s41598-025-17551-8.

Correspondence and requests for materials should be addressed to B.A. or M.P.

Reprints and permissions information is available at www.nature.com/reprints.

Publisher's note Springer Nature remains neutral with regard to jurisdictional claims in published maps and institutional affiliations.

Open Access This article is licensed under a Creative Commons Attribution-NonCommercial-NoDerivatives 4.0 International License, which permits any non-commercial use, sharing, distribution and reproduction in any medium or format, as long as you give appropriate credit to the original author(s) and the source, provide a link to the Creative Commons licence, and indicate if you modified the licensed material. You do not have permission under this licence to share adapted material derived from this article or parts of it. The images or other third party material in this article are included in the article's Creative Commons licence, unless indicated otherwise in a credit line to the material. If material is not included in the article's Creative Commons licence and your intended use is not permitted by statutory regulation or exceeds the permitted use, you will need to obtain permission directly from the copyright holder. To view a copy of this licence, visit http://creativecommons.org/licenses/by-nc-nd/4.0/.

© The Author(s) 2025